THESIS FOR THE DEGREE OF LICENTIATE OF ENGINEERING

Plasmonics with a Twist

ROBIN OGIER

Department of Applied Physics
CHALMERS UNIVERSITY OF TECHNOLOGY
Göteborg, Sweden 2014

Plasmonics with a twist
ROBIN OGIER

Department of Applied Physics
Chalmers University of Technology
SE-412 96 Göteborg
Sweden
Telephone +46 (0)31 772 1000

Cover:
Left: Spin angular momentum transfer of photons to a bead trapped in a right-handed circularly polarized focused light beam.
Right: Right-handed circularly polarized light impinging on a right-handed silver tetramer.

Chalmers reproservice
Göteborg, Sweden 2014

Plasmonics with a Twist

Robin Ogier
Department of Applied Physics
Chalmers University of Technology

Abstract

This thesis focuses on the exploration of interactions between circularly polarized light and plasmonic nanostructures, and nanoparticles. Polarization is an integral part of light and has a wealth of applications in the modern world. Circularly polarized light in particular interacts in a specific way with the foundation of life itself: the amino-acids, among which 23 are chiral. These amino-acids exhibit an optical activity. However this phenomenon is weak due to the weak coupling of molecules to an external light field. Plasmonic particles, on the other hand, have strong interactions with an external light field. They could therefore be perfect candidates in manipulating light polarization and interactions with chiral molecules. Two paths were taken in the use of circularly polarized light: one was to transfer spin angular momentum from the circularly polarized light to get the highest spinning frequency possible of a trapped particle, the other was to fabricate structures with high circular dichroism in the visible.

Nanoparticles in the form of gold spheres were trapped in aqueous solution by a 2D optical trap as described in Appended Paper I. By using a circularly polarized light beam for the trapping, it is possible to set these particles into a rotational motion. The reason for this rotation is the transfer of the spin angular momentum of the incident photons to the absorbing particle. Frequencies of several kHz, the highest reported in literature for particles in water, were recorded during the experiments. The results are well explained by classic electromagnetism theory and hydrodynamic theory. The maximum spinning frequency is reached at equilibrium between the external torque induced by the transfer of spin angular momentum, and of the frictional torque originating from the viscosity of the surrounding medium. It is worth noting that this viscosity is reduced in the immediate vicinity of the particle by the particle heating due to the use of high laser power. The transfer of spin angular momentum is put in evidence by an increase of the rotational frequency as the laser power is increased. However at high power, both temperature and friction increase, which leads to an increase of the influence of the stochastic torque on the particle motion.

In Appended Paper II, right- and left-circularly polarized light were used as means of characterization of the circular dichroism (CD) of nanofabricated metal structures. The CD is a measure of the chiral optical response of a material. The structures showing the strongest CD in the visible to near-infrared wavelength range were closely packed silver tetramers that consist of four disks of increasing heights. They were realized based on both the hole-mask colloidal lithography technique and angular metallic evaporation. It provided us with a simple fabrication technique for obtaining a uniform coverage of large areas. The finite element method (Comsol) and the coupled-dipole approximation were used to investigate the origin of this strong CD. It originates in strong near-field interactions between the particles caused by the small interparticle distances, combined with the 3D nature of the arrangement of the four nanodisks. The gaps present within each structure could be of interest in future molecular analysis applications.

Keywords: Nanoparticles, optical tweezers, colloidal lithography, nanofabrication, chirality, plasmonic nanostructures, particle spinning

APPENDED PAPERS

The following papers are included in this thesis:

Paper I: *Ultrafast spinning of gold nanoparticles in water using circularly polarized light.*
Lehmuskero, Anni; OGIER, ROBIN; Gschneidtner, Tina; Johansson, Peter; Käll, Mikael
Nano Letters. 2013 vol. 13 (7) pp. 3129-3134

My contribution: I participated in the measurements and in the discussion of the results. I also participated as a co-author in writing the paper.

Paper II: *Macroscopic layers of chiral plasmonic nanoparticle oligomers from colloidal lithography.*
OGIER, ROBIN; Fang, Yurui; Svedendahl, Mikael; Johansson, Peter; Käll, Mikael
ACS Photonics. 2014 *Accepted Manuscript*

My contribution: I used HCL to fabricate the chiral plasmonic structures. I participated in the simulations of the nanostructures and discussed the results. I wrote a draft of the paper.

Contents

Chapter 1

Introduction

Nanoplasmonics forms a part of the bigger field of nanophotonics. It describes how electromagnetic fields can be confined to dimensions whose order is around the same, or smaller than the wavelength. It was in already in 1900 that Paul Drude demonstrated how an electron gas in a bulk metal could support a collective electron oscillation known as plasma oscillation. Such oscillations are more commonly called plasmons. However, despite the apparent simplicity in the description of surface plasmon polaritons and localized surface plasmons by classical physics, it is often hard to accurately evaluate the extrications of many phenomena in nanoplasmonics. Throughout the 20th and 21st centuries, plasmons have been explored and exploited in a number of ways.[1–3]

One aspect of light that can be manipulated by making use of plasmons is its polarization.[4–7] The ability to manipulate the polarization of light is essential for numerous applications including spectroscopy, microscopy, telecommunications, etc. One of its earliest applications was probably the use of Iceland spar (see Figure 1A) by navigators to tell the direction of the sun in cloudy and twilight conditions. Since then, many advances have been made to further the understanding of the interaction between light polarization and objects at the micrometre and nanometre scales.[8] Though linearly polarized light has been a subject of choice and explored extensively, circularly polarized light (CPL) has received less attention.

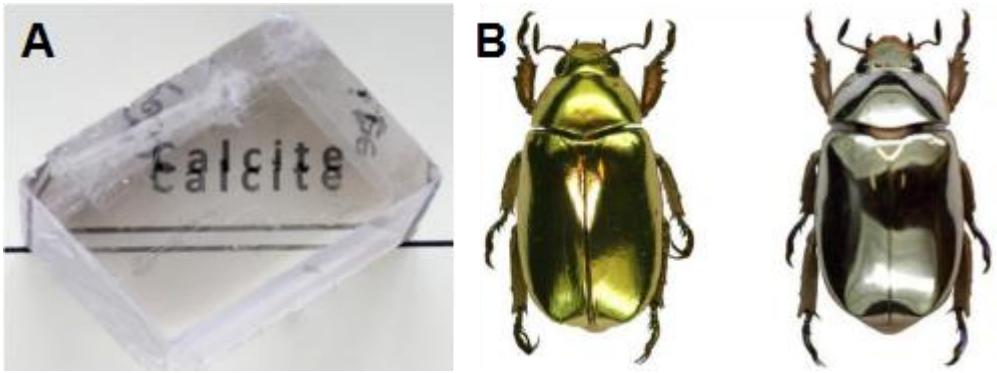

Figure 1: A) Picture of a piece of Calcite crystal whose birefringence splits horizontal and vertical linearly polarized light. B) Pictures of the *Chrysina aurigans* (left) and the *Chrysina limbata* (right) beetle specimens having different reflection values of their chitin depending on the handedness of the impinging CPL and displaying their golden- and silver-like appearance, respectively.[9]

Everyday around us and inside us, there are objects that are interacting differently depending on the handedness of the circularly polarized light impinging on them. They are called chiral. All amino-acids are chiral, as well as DNA, many molecules, or the wings of some beetles (see Fig. 1B). Getting information about the handedness of molecules is important in the development of effective drugs; but the intricacies of how circularly

polarized light interferes with such chiral objects is interesting in a fundamental way and will help in designing artificial chiral structures, or enantiomer-specific sensors.[10]

Probing and observing the optical forces exerted by light on matter has been brought within reach thanks to optical trapping.[11,12] Optical tweezers techniques have been used for over 20 years to manipulate and study the properties of micron-sized particles. The ability to achieve displacements with a nanometre accuracy and measure forces down to the piconewton has opened up new areas of study in biology and physics such as the observation of single molecule,[13] DNA properties,[14] and single metallic particles. Trapping of metallic particles is not a challenge anymore.[15] Rotation of single plasmonic nanostructures in laser tweezers has also been demonstrated.[16] However the limits of how fast a trapped plasmonic nanoparticle can spin is still an interesting subject to dwell upon.

Imitating nature at the nanoscale is the domain of nanofabrication. Nanoscale objects can be fabricated through top-down fabrication methods like electron-beam lithography (EBL),[17] or bottom-up fabrication like colloidal lithography.[18] Though EBL allows great control over nanostructures design, we prefer to it colloidal lithography. It is a very versatile method for fabricating square centimetre areas of clusters of nanoparticles, nanorings, nanoholes, etc. whose behaviour can be modelled via different calculation methods such as coupled-dipole approximation (CDA), or finite element method (FEM). Using these tools, we can realize artificial plasmonic chiral structures on the model of molecules. Their understanding would provide a useful knowledge about the development of an enantiomer-specific sensing platform based on arrays of such handed plasmonic nanoparticles.

In this thesis, the aim was twofold: **1)** achieving the highest rotational speed of a metallic nanoparticle trapped in a circularly polarized laser beam and finding the limiting factor, **2)** fabricating plasmonic chiral structures with a strong chiral optical activity suitable to be used for sensing and unfolding the interactions involved.

The outline of the thesis is the following. Chapter 2 describes circularly polarized light, the basis of optical trapping and the properties of chiral structures with examples from the literature. Chapter 3 is centred on the optical trapping experiments and provides details about sample preparation, and optical characterization methods. Chapter 4 focuses on plasmonic chiral nanostructures and presents the nanofabrication of the structures, optical characterization methods, and simulation methods. Chapter 5 gives a summary and future outlook of the research field.

Chapter 2

Background

Given the fact that the phenomenon of light can be explained by the wave-particle duality theory, interpretations of light polarization and its interactions with plasmonic objects can be emphasized from either viewpoints. Both pictures have already been adopted in the field of plasmonics.[19,20] This chapter will establish the basics of these two complementary aspects of handed light in the context of some examples relevant to my own research.

2. 1. Circularly polarized light

When considering light in terms of electromagnetic plane waves, defining circularly polarized light is straightforward. A linearly polarized wave has its orientation defined by the direction of its electric field wave vector which is confined to a single plane along the direction of propagation. For a circularly polarized wave, the electric field vectors have constant amplitude but their direction rotate continuously perpendicular to the direction of propagation. A circularly polarized wave can also be described by two linearly polarized waves of equal amplitude with a phase retardation relative to each other of $\pm \pi/2$. If the two linearly polarized waves have different amplitudes, or if their relative phase retardation is different than $\pm \pi/2$, then we have elliptically polarized light. To establish a convention for the rest of this thesis, we will define the handedness of circularly polarized light (CPL) as viewed from the source. While looking from the source, if the electric vector of the light going away from you rotates clockwise (respectively counter clockwise), the light will be right- (respectively left-) circularly polarized (RCP/LCP).

On the other hand, light is also a beam of photons. Each photon has a linear momentum $\hbar k$ directed along the beam axis perpendicular to the wavefronts, and an energy $\hbar\omega$. In addition, each photon has a spin angular momentum of $\hbar$ aligned parallel (LCP) or antiparallel (RCP) to the direction of propagation. In the case of a CPL beam, all photon spins possess the same alignment.

As we will see its implications later in this chapter, light can carry angular momentum without being circularly polarized. A light beam can carry an *orbital* angular momentum which is independent from the light polarization. For example, Laguerre-Gaussian beams (see Figure 2) that have l intertwined helical wavefronts have a wavector spiralling around the beam axis. It adds to the photon momentum an azimuthal component. Thus each photon gets an orbital angular momentum of $l\hbar$. The orbital angular momentum has been exploited with the same aim as in Appended Paper I to spin plasmonic nanoparticles via optical tweezers in the literature.[21] A vortex beam can additionally be used as a microtool in engineering chiral nanostructures.[22] Transfer of angular momentum

from spin to orbital angular momentum is an interesting subject in the studies of circularly polarized light interactions with plasmonic nanoparticles.

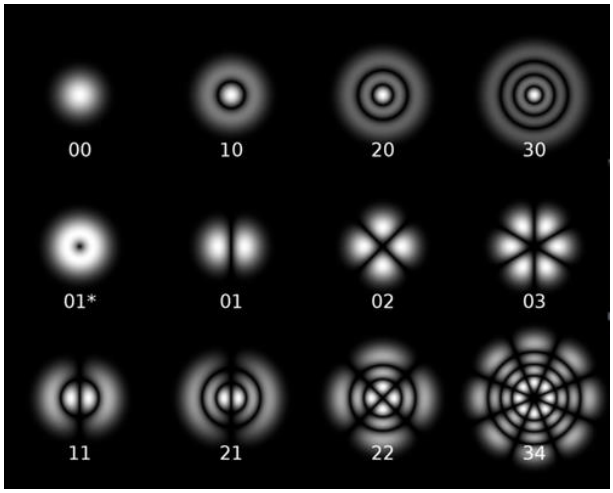

Figure 2: Intensity profiles of twelve Laguerre-Gaussian modes LG(p, l) where p is the radial index, and l is the azimuthal index of the Laguerre polynomials used to describe them.

2. 2. Optical forces

The first step in investigating CPL was to be able to observe the transfer of angular momentum of light to matter. One of the first experiments allowing that was performed in 1936 by Beth.[23] He used a quarter-wave plate suspended from a quartz fibre to transform circularly polarized light to linearly polarized light. During the process, the spin angular momentum of light was removed from each photon and transferred to the quarter-wave waveplate in the form of a measureable torque.

Transferring angular momentum to a particle instead, is a different challenge. An absorbing particle will absorb both the angular and linear momentum from a light beam. Attributing a displacement of the particle to either momentum contribution is a hard task to perform. Keeping the particle in a stable position is needed. To solve this problem, the use of optical forces provided by optical tweezers are the key. The work by Ashkin et al.[24] has opened the path to the development of optical trapping of microscopic particles including biological specimens. It then became a tool with numerous applications in biology (microrheology, local heating, single cell manipulation, etc.), and physics. Optical trapping of nanoparticles, instead of micrometre-sized particles, is more challenging due to the limited amount of force one light can exert on such dimensions.

2. 2. 1. Optical trapping of plasmonic nanoparticles

The mechanical forces, *i. e.* radiation pressure, applied by light on objects it interacts with have been explained by Maxwell's theory of electromagnetism in the 19th century. In the case of a particle, one can understand the radiation pressure as a natural consequence of the conservation of momentum during absorption and scattering of photons. In dielectric materials, electromagnetic fields induce a polarization which translates to a gradient force directed towards high intensity field regions. Focusing strongly a laser beam, for example, is a method through which we can obtain gradient forces strong enough

to trap individual dielectric micro- and nanoparticles. Figure 3 illustrates this simple principle.

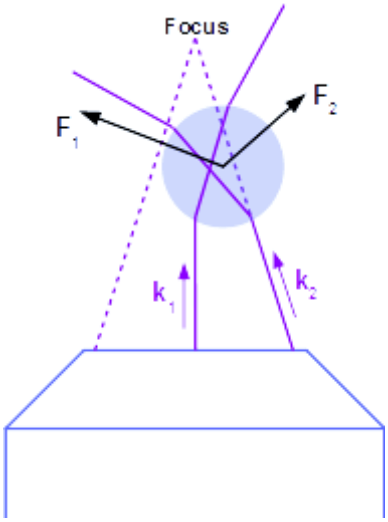

Figure 3: A dielectric bead is in the path of a focused laser beam. Two rays from the beam with wave vectors k_1 and k_2 are represented. The rays apply forces F_1 and F_2 when refracted on the surface. The resulting gradient force pulls the bead towards the focus of the laser beam.

In optical tweezers for dielectric particles, gradient force is dominating. Comparatively, metallic nanoparticles strongly absorb and scatter light close to their localized surface plasmon resonance (LSPR). This causes the scattering forces to increase, and decreases the trap stability. Nonetheless, off-resonant optical tweezers can reliably trap metallic nanoparticles as seen in the literature.[12] The following theoretical considerations allow a better understanding of different concepts in the trapping of plasmonic nanoparticles.

Optical properties of noble metals can be described by the complex dielectric function $\varepsilon_m(\omega)$. This dielectric function can be approximated by the Drude-Lorentz model which comprises two major contributions: the electronic interband transitions, and the quasi-free movement of the conduction band electrons.

$$\varepsilon_m(\omega) = \varepsilon_r - \frac{\omega_p^2}{\omega^2 + i\omega\Upsilon} + \frac{\Delta\varepsilon\Omega_p^2}{\Omega_p^2 - \omega^2 - i\Gamma\omega} \tag{1}$$

In this relation, ε_r describes the relative permittivity at high frequencies, ω_p is the resonant plasma frequency, Υ is the damping factor, $\Delta\varepsilon$ is the oscillator strength, Ω_p and Γ are respectively the plasma frequency and the damping factor for the bound electrons.

Upon illumination, a nanoparticle both absorbs and scatters light in ways expressed by the scattering, absorption, and extinction cross sections. If we consider a metallic sphere of radius a much smaller than the incident wavelength in vacuum (within the quasi-static approximation), surrounded by a medium of dielectric constant ε, and excited by a uniform external electric field, we can describe this system by an induced dipole moment whose complex polarizability is the following:[25]

$$\alpha(\omega) = 4\pi a^3 \frac{\varepsilon_m(\omega) - \varepsilon}{\varepsilon_m(\omega) + 2\varepsilon} \tag{2}$$

This complex polarizability expresses a resonant condition reached when $Re[\varepsilon_m(\omega)] = -2\varepsilon$. It can also be used to calculate, via the Poynting vector, the scattering, absorption, and extinction cross sections of a plasmonic nanostructure.[1]

$$C_{sca} = \frac{k^4}{6\pi}|\alpha|^2 \tag{3.a}$$

$$C_{abs} = k\, Im[\alpha] \tag{3.b}$$

$$C_{ext} = C_{sca} + C_{abs} \tag{3.c}$$

Both characteristics of the laser and the nanoparticle will impact on the forces acting on a nanoparticle in a focused laser beam. The time averaged force $< \vec{F} >$ on a particle due to harmonic fields can be calculated by integrating the Maxwell's stress tensor, $\overleftrightarrow{T}$, over a closed surface surrounding the particle (δV):

$$< \vec{F} > = \int_{\delta V} < \overleftrightarrow{T}(\vec{r}, t) > \vec{n}(\vec{r}) da \tag{4}$$

, where $\vec{n}$ is the unit normal to δV, and da is an infinitesimal surface element. From this equation, it is possible to develop an analytical expression of the optical forces in the case of a small spherical particle within the quasi-static approximation. Considering a dipolar particle illuminated by a monochromatic EM wave, the time-averaged induced forces acting on this dipole can be derived from the nonrelativistic Lorentz force and split into two components, the gradient and the scattering forces:[26]

$$< \vec{F} > = < \overrightarrow{F_{grad}} > + < \overrightarrow{F_{scatt}} > \tag{5.a}$$

$$< \overrightarrow{F_{grad}} > = \frac{1}{4}\varepsilon_0 \varepsilon\, Re[\alpha] \nabla\left(\vec{E}^* \vec{E}\right) \tag{5.b}$$

$$< \overrightarrow{F_{scatt}} > = \frac{1}{2}\varepsilon_0 \varepsilon\, Im[\alpha] Im\left(\sum_s E_s^* \nabla E_s\right) \tag{5.c}$$

, where the sum is over $s = x, y, z$. The gradient force comes from the intensity profile gradient of the laser beam and is proportional to the dispersive part of the complex polarizability α. The scattering force comes from the momentum transfer from the external field by scattering and absorption to the nanoparticle and is proportional to the dissipative part of the polarizability. Since the gradient force pushes the nanoparticle towards the intensity maxima of the field and the scattering force pushes the particle in the direction of light propagation, we need $< \overrightarrow{F_{scatt}} > \ll < \overrightarrow{F_{grad}} >$ to achieve a trap in 3D. From these considerations, it is quite straightforward from the calculation of the different components of a nanoparticle complex polarizability to choose a proper wavelength to achieve trapping. Close to the plasmon resonance, the imaginary part dominates, leading to a strong scattering force pushing the nanoparticle in the direction of light propagation. Off resonance, one can either get repulsive (negative) gradient forces by being blue-shifted respective to the resonance of the particle, or attractive gradient forces by being red-shifted respective to the plasmon resonance. These considerations are important if we want to achieve transfer or angular momentum thanks to a Laguerre-Gaussian beam. Of course, in the case of a 2D trap, the scattering force has a less constraining influence. To summarize, by combining all the above expressions, it is possible to calculate the optical forces exerted on a plasmonic nanoparticle.

2. 2. 2. Transfer of angular momentum

Now that we know the basics about nanoparticle manipulation, we can take a look at the types of interactions possible between spin angular momentum (SAM), orbital angular momentum (OAM), and plasmonic nanostructures.

As seen before, Laguerre-Gaussian beam can be a source of OAM.[27] They are usually identified as LG(p, l), where l corresponds to the azimuthal term, and (p + 1) is the number of radial nodes. Their helical wavefronts are supposed to carry for linearly polarized light an OAM of $l\hbar$ per photon. For a tightly focused beam, the total angular momentum of a Laguerre-Gaussian beam can be calculated from Maxwell's equations within the paraxial approximation and is equal to:

$$\left[l + \sigma_z + \sigma_z\left(\frac{2kz_r}{2p + l + 1} + 1\right)^{-1}\right]\hbar \tag{6}$$

, where $\sigma_z = 0, \pm 1$ for linearly and circularly polarized light respectively, k is the light wave number, and z_r is the Rayleigh range. So by using both OAM and SAM it is possible to slow down or accelerate the rotational speed of a trapped particle.[28] Such transfers have already been reported by different authors using trapping relying on radiation pressure of a circularly polarized Laguerre-Gaussian beam. A general conclusion from their works is that in order for the spin and orbital angular momentum of photons to interact in a significant manner with the trapped particle, absorption must be the dominant mechanism for the transfer of angular momentum.[12]

However ultimately, the maximum rotational speed is limited by the viscosity of the medium surrounding the nanoparticle. For a sphere rotating around a single axis whose rotation is driven by an external torque induced by the incident light, the equation of motion is the following:

$$J\frac{d\omega}{d\tau} = M_{ext} + M_f + M_s \tag{7}$$

, where $J = 2mR^2/5$ is the moment of inertia of a sphere of mass m and radius R, ω is the instantaneous angular velocity of rotation, M_f is a friction torque related to the viscosity of the surrounding medium and proportional to ω, and M_s is the stochastic torque. The external torque caused by the SAM transfer is linked to the absorption cross-section through $M_{ext} = IC_{abs}/\omega_0$ with I being the light intensity. The viscous frictional torque is linked to the dynamical viscosity η of the liquid and follow the Stokes equation to give $M_f = -8\pi R^3/\omega$. At equilibrium of the torques, that is to say when $M_{ext} = -M_f$, we reach an average angular velocity Ω. This condition leads to the expression of the following average rotational frequency f:

$$f = \frac{C_{abs}I}{16\pi^2\eta R^3\omega_0} \tag{8}$$

It can be noticed that this frequency depends on the viscosity of the liquid η, which itself depends on the temperature of the liquid and can be estimated from the following equation for a laminar flow:

$$\eta(T) = \eta_0 \exp\left[\frac{E_a}{N_A k_B (T - T_0)}\right] \tag{9}$$

, where η_0 is the viscosity of the surrounding medium at T = 140 K, E_a is an activation energy, k_B is the Boltzmann's constant, N_A is the Avogadro number, and T_0 is a temperature offset. From this equation, two applications of rotation of nanoparticles in optical tweezing are apparent: viscosity measurement,[29] and temperature sensing.[30] But temperature itself can be a problem as it is depending as well from the absorption cross-section and the temperature increase from ambient temperature is $\Delta T = C_{abs} I / 4\pi R\kappa$, where κ is the thermal conductivity of the surrounding medium. Indeed previous work on trapping experiments reported water medium temperatures going over the boiling point.[31,32]

So far we considered the spin angular momentum and the orbital angular momentum to be independent. This is true in general. SAM is normally associated with the polarization of the optical field, and OAM is associated to its phase. Using anisotropic and inhomogeneous medium, they can be made to interact and a change in both polarization and phase of the beam will occur. Such optical elements that allow this phenomenon are called Pancharatnam-Berry phase optical elements. Examples of such optical elements can already be found and include *q*-plates, liquid-crystals systems, etc. Plasmonic metasurfaces are also capable of spin-to-orbit coupling in the visible and phase control.[33] They rely on manipulating locally the optical field by nanoantennas such that the field gets a different phase retardation at each nanoantenna. The overall control of the optical field is achieved by the arrangement of different nanoantennas on the substrate. One can also use identical antennas to control the beam's phase-front as in Figure 4.[34]

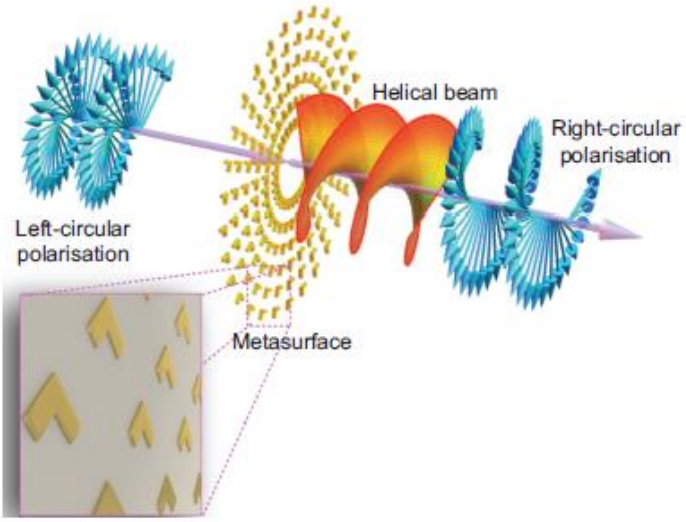

Figure 4: Schematic representation of spin-to-orbit coupling through a metasurface. By switching the polarization of the incident beam from left- to right-handed circularly polarized light thanks to the metasurface in inset, the conservation of angular momentum demands that the change in the SAM will be transferred to OAM because of the rotational invariance of the metasurface.[34]

By designing a nanoantenna so that the two orthogonal linear polarizations experience a π optical retardation, one can switch the handedness of an incident circularly polarized light. And then by designing the arrangement of these individual nanoantennas, one can dictate the interaction between SAM and OAM through the conservation of angular momentum.

We have already seen that due to the conservation of angular momentum, we can induce rotation to spherical particles via the transfer of SAM.[35] Moreover, careful engineering of plasmonic nanostructures allows to induce phase retardation on incident light. Going further, phase retardation can also be made to vary within a single structure

and produce a mechanical torque. Phase retardation variations within a single object will produce an orbital angular momentum on the scattered light, which itself, still via the conservation of angular momentum, will apply a torque on the plasmonic nanostructure and cause its rotation.[36] An example of such a structure can be found in Figure 5 and is the assembling of four of the nanoantennas from Fig. 4.

Figure 5: Example of design of a light-driven motor in a gammadion shape. The symmetry of the structure allows it to induce angular momentum from a linearly-polarized plane wave thanks to patterning of the phase retardation within the structure.

To maximize the generation of the optical torque, one must work at an illumination wavelength where the phase retardation is equal to $\pm\pi/2$ which depends on the different plasmonic modes of the nanostructure. Overall, one can induce angular momentum via a single nanostructure through the modification of the phase retardation of the incident light within this structure. This is made possible by a simple geometrical consideration on the shape of the object; one must break the symmetry of the nanostructure in the plane of incidence.

CPL can be influenced upon by plasmonic nanostructures. Metamaterials can bridge the gap between orbital and spin angular momentum by careful design of the nanoparticles geometry, as seen in Fig. 4. Furthering the considerations of its geometrical concepts to a single structure extends towards the creation of a rotating particle by induced orbital angular momentum if the particle has some movement freedom (as seen in Fig. 5), or towards the fabrication of planar chiral metamaterials generating chiral fields.[10] From spin angular momentum to orbital angular momentum, from spinning nanoparticle to chiral nanoparticle, the same geometrical considerations seen in the previous paragraphs are followed.

2. 3. Chirality

Chirality is the name linked to this simple geometrical property: a chiral object cannot be superimposed with its mirror image. For molecules, the two symmetric compounds are called the two enantiomers. Chirality can manifest itself as optical activity. A chiral structure will have a different response to left- or right-handed circularly polarized light. Different phenomena happen when circularly polarized light interacts with chiral structures, such as circular dichroism or optical rotary dispersion. Many things around us are chiral: the essential amino-acids, proteins, nucleic acids, biomolecules, etc. All essential amino-acids have the same handedness. A lot of research has been devoted to the origin of chirality.

Although chiral molecules are optical active, the chiral optical phenomenon is weak. It is due to how the small dipole moments of molecules couple weakly with an external light field. Thus, it is difficult to discriminate optically enantiomers which is essential in the development of drugs. Plasmonics, due to their high interactions with an external light field, could help in overcoming this hurdle. Based on the same design as in Fig. 5, it has

been demonstrated that plasmonic nanostructures can have significant chiral optical activity.[10]

2. 3. 1. Definition of Chirality

True chiral structures are three-dimensional. In order to create artificial chiral plasmonic structures, we can go through two different geometrical paths depicted in Figure 6.

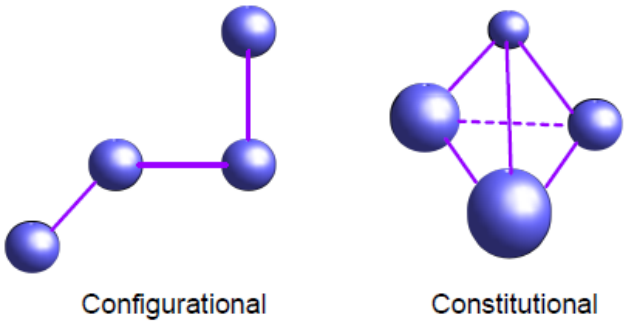

Figure 6: Two different chiralities from a geometrical point of view. On the left, the 4 spheres are identical but are placed in space in a handed manner; it is configurational chirality. On the right, the 4 spheres are different but are placed at the corners of a regular tetrahedron; it is constitutional chirality.

These two same geometries are present in chemistry, but due to its mechanical stability, constitutional chirality is more commonly found. Both strategies can be implemented by plasmonic nanostructures. However, because of the fact that coupling efficiency between the different elements will define the strength of a CD signal, it is generally preferable to choose a geometry where coupling is facilitated. The configurational geometry having identical individual elements, their resonance will be the same and will translate to efficient plasmon couping.

In order to characterize how chiral a structure is, different evaluation methods are available. The circular dichroism (CD) is the one normally used. CD is defined for molecules as the difference in absorbance between left- and right-circularly polarized light passing through a sample.

$$\theta\,(\mathrm{deg}) = \Delta A\left(\frac{\ln 10}{4}\right)\left(\frac{180}{\pi}\right) \tag{10}$$

, where $\Delta A = A_{LCP} - A_{RCP}$, and θ is the ellipticity. However considering only absorbance is not valid for plasmonic nanoparticles and one must use the original definition of CD:

$$\tan\theta\ (rad) = \frac{I_{RCP}^{1/2} - I_{LCP}^{1/2}}{I_{RCP}^{1/2} + I_{LCP}^{1/2}} \tag{11}$$

, where I is the intensity of light passing through the structure for right- and left-circularly polarized light. Another similar quantity, the dissymmetry factor g, is utilized in chemistry to quantify the chiroptical response of a medium. It is defined as follows:

$$g = \frac{I_{LCP} - I_{RCP}}{\frac{1}{2}(I_{LCP} + I_{RCP})} \tag{12}$$

This factor is a dimensionless quantity useful to compare the signs and magnitudes of CD signals between different kinds of samples, conditions, and excitation wavelengths.

In naturally occurring chiral optical material, if circularly polarized light interacts with a chiral molecule, it causes a displacement in the electron clouds of the molecule from its equilibrium position in a helical fashion. Due to the helical behaviour of these displacement currents, there is an induced magnetic moment created comporting a component parallel to the regular electric dipole moment and in the direction of light propagation. This gives rise to a particular interaction between circularly polarized light and the molecule. If circularly polarized light interacts with a similar plasmonic "molecule", there will be some strong displacement currents between the elements of this "molecule" due to the high number of electrons present in metallic particles. Thus, the generation of localized plasmons will cause strong chirality in artificial chiral plasmonic structures compared with molecules.

2. 3. 2. Chirality vs. Polarization conversion

True three-dimensional chirality comes from the uniaxiality of the structure, as compared to biaxial structures that achieve polarization conversion. Uniaxiality is reflected into the optical properties of the structure. Upon comparison of CD measurements from two opposite directions of illumination, a true chiral object should have identical signals. In the case of polarization conversion, the (biaxial) material is birefringent upon the two main axis of the lattice polarization. If there is a change in the illumination direction, then the sign of the polarization conversion should change. Consequently, instead of two identical CD signals, we would obtain two CD signals mirrored at the 0 line. Depending on the strength of the signal, one can consider the chiral signal and the polarization conversion to be purely additive (low strength signals) and a simple comparison of the CD spectra measured from two opposite directions would allow the separation of these contributions.[17]

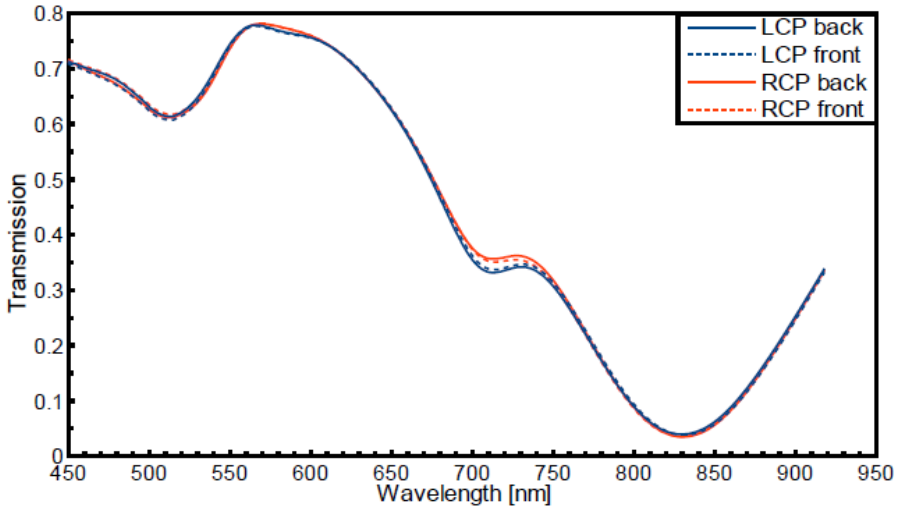

Figure 7: Experimental transmission spectra upon illumination with LCP (blue line) and RCP (red line) with a normal incidence upon the back (continuous line) and front (dashed line) side of the sample substrate. The sample substrate is covered with RH silver tetramers described in Appended Paper II. The superposition of the respective back and front signals proves the uniaxiality (and the true chirality) of the structure.

Figure 7 depicts an example of a true chiral uniaxial structure whose complete details are described in Appended Paper II. Indeed, there is no change in the line shape of

the signals upon changing the illumination direction. This dismisses the presence of polarization conversion occurring in the structure.

2. 3. 3. Superchirality

As already mentioned, enantioselective signals are typically quite small. It was proposed that, as plasmonic local field enhancements can be used to increase the interaction between light and the electronic, vibrational, and rotational resonances of molecules, superchiral electromagnetic fields would enhance interactions with chiroptical resonances of molecules. Various theoretical aspects of superchiral light have already been investigated.[37,38]

The optical chirality C was defined originally by Lipkin:[39]

$$C = \frac{\varepsilon_0}{2}\boldsymbol{E}.\boldsymbol{\nabla}\times\boldsymbol{E} + \frac{1}{2\mu_0}\boldsymbol{B}.\boldsymbol{\nabla}\times\boldsymbol{B} \tag{13}$$

, where ε_0 and μ_0 are the permittivity and permeability of free space, respectively, and $\boldsymbol{E}$ and $\boldsymbol{B}$ are the local electric and magnetic fields. To determine the enantioselectivity of a system, we can come back to the expression of the dissymmetry factor g defined in equation (12). For a chiral molecule, g is linked to the optical chirality by the following equation:[38]

$$g = g_{CPL}\left(\frac{cC}{2\omega U_e}\right) \tag{14}$$

, where g_{CPL} is the dissymmetry factor for a CPL, c is the speed of light, and U_e is the time-averaged electric energy density. From this equation, we can deduce that to enhance the enantioselective dissymmetry factor, the field chirality term (in parenthesis) can be increased either by decreasing the electric field energy density,[40] or by increasing the optical chirality C.[41] Chiroptical activity such as circular dichroism and optical rotation may generate local fields with enhanced optical chirality. From literature,[42] the main contributions come from electric dipole-magnetic dipole interactions, and electric-dipole-electric quadrupole interactions.

Plotting the optical chirality of chiral structures in Figure 8 shows how the optical chirality is locally enhanced with respect to the optical chirality of CPL. But despite high enhancements, this structure wouldn't be suitable for enantiomer sensing due to averaging of positive and negative enhancements. One would have to design structures with the generation of chiral near-fields with a dominant handedness to achieve enantioselective sensing.[43]

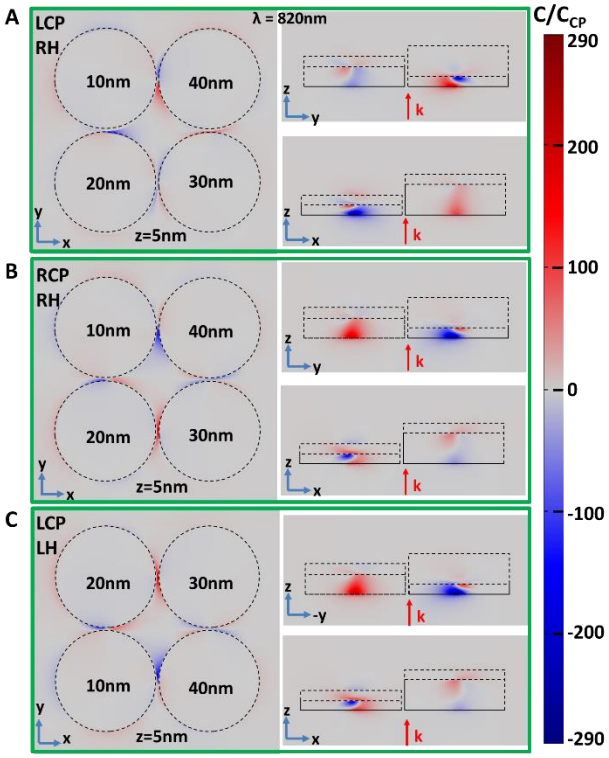

Figure 8: Simulated optical chirality enhancement factor of silver tetramers from Appended Paper II in vacuum on a glass substrate based on the finite element method (FEM). A) Optical chirality enhancement factor at 820nm of a RH tetramer for LCP light, and B) RCP light. C) Same as in A), but for a LH tetramer. Superchiral fields with a maximum enhancement of 2 orders of magnitude are created locally.

Chapter 3

Methods and characterization in optical trapping

3. 1. Sample preparation

In optical trapping experiments, especially with trapping metallic nanoparticles, the trapped object will be pushed on a glass coverslip to complete the immobilization. The surface it is pushed on must be cleaned in a specific way to avoid unwanted interactions from objects alien to the experiment like dust particles. The cleaning method adopted in the Appended Paper I is using a solution called TL1 as a cleaning agent. A TL1 solution is a mix of purified water, hydrogen peroxide, and ammonium in the ratio 3:1:1. After passing the glass coverslips under a stream of nitrogen to remove the biggest dust particles, these coverslips are put into this solution at a temperature of 80°C for 15 min. Precautions are needed. One has to cover the recipient during the incubation period, and all manipulations must be done under a hood due to the emission of harmful fumes. After a 15 min incubation period, the glass coverslips are rinsed with purified water and blow-dried under a stream of nitrogen. By using this method, we observed that rotation could be more easily achieved than with the cleaning method used in step 1 of the paragraph 4. 1. 1.

Once the cleaning finished, a colloidal solution of gold particles (average radius 200 nm) is diluted in purified water to reach concentrations low enough to avoid multiple trapping events. 3µL of this diluted solution is pipetted into an adhesive well (100 µm thick) placed onto a glass coverslip. A second glass coverslip will complete the sample and seal our well.

3. 2. Optical characterization

3. 2. 1. Dark-field microscopy

Dark-field microscopy is used in our trapping setup to identify the position of the gold colloids. It is based on the fact than upon illumination, objects scatter light in directions different than the illumination direction. Illumination is done by a dark-field condenser with a numerical aperture (NA=0,8) higher than the one of the objective collecting the light (NA=0,7). Light that has not interacted with objects will not be collected by the imaging objective. Some of the scattered light will reach the objective and be directed to the image plane. Scattering particles will then brightly appear on a dark background.

3. 2. 2. Avalanche photo-diode (APD) and auto-correlation function

To follow accurately the trapped gold colloids (see Figure 9) rotation, the collected light is sent to a fibre-coupled APD. It permits to have a higher sensitivity than a standard photodiode and performs well for low-level light detection and photon counting. These high performances are due to the internal gain mechanism of the APD. Absorption of incident photons creates electron-hole pairs. Under strong internal electric fields these electrons are accelerated and produce secondary electrons by impact ionization. This phenomenon is the "avalanche" responsible for the high sensitivity.

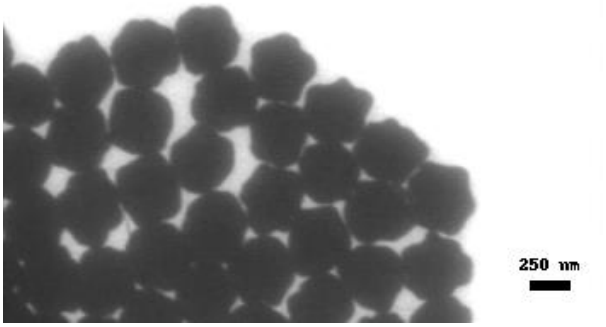

Figure 9: TEM image of the gold particles. Their average radius is around 200 nm. We can see that their surface present some irregularities which will be used to track their rotational speed.

In Fig. 9 we notice that the colloids are not perfect spheres. While rotating, the deformations will create a periodical variation of the light intensity detectable by the APD. Other intensity variations will be added to the collected data such as caused by the Brownian motion of the particle.

The auto-correlation function allows to distinguish between the different contributions to the intensity variations. It measure the correlation of a signal with itself shifted in time by some delay. This function is expressed as following:

$$C(\tau) = \frac{1}{t-\tau}\int_0^{t-\tau} x(t)x(t+\tau)dt \qquad (15)$$

, where τ is some time delay, and *x(t)* is a signal. The auto-correlation function can be used to detect periodicity in a signal such as the spinning frequency in our case. The period of the auto-correlation corresponds to the period of the intensity signal. If there is noise in the signal, the envelope of the auto-correlation function decreases exponentially (see Figure 2 of Appended Paper II). In our case, the envelope is correlated to the stochastic motion of the particle and exponentially decays with a characteristic correlation time τ_0.

3. 2. 3. Optical trapping setup

The optical tweezers are built around an inverted microscope (Nikon TE300), and a white-light dark-field illumination from a halogen lamp is used for localization of the particles. Figure 1a in Appended Paper I is a schematic of the whole setup. A near-infrared laser (λ=830 nm) will be the source for the trapping beam. From the laser, the beam passes through a laser-line filter and a beam expander to get a beam of light filling the back aperture of the objective. This light beam gets circularly polarized by passing through a

linear polarizer and a quarter-wave plate. It is then reflected by a dichroic beamsplitter and focused by an objective (60X; NA=0,7) to trap the gold colloids.

The scattered light from the colloids from dark-field illumination is collected by the objective, passes through the dichroic beamsplitter and a hot mirror to remove contributions from the laser light, and is collected by a fibre-coupled avalanche photo diode (APD) before being analysed by an autocorrelator. Due to the irregularities of the particles on Fig. 9, the scattered light by a single particle is dependent on its position. By tracking the periodical variations of the light intensity due to this anisotropic scattering, one can deduce the rotation frequency of the trapped particle.

Chapter 4

Plasmonic chiral nanostructures

4. 1. Sample preparation

The nanofabrication technique used in the Appended Paper II for the fabrication of the artificial chiral samples is hole-mask colloidal lithography (HCL). HCL is a relatively simple technique that can be used to produce large areas of nanostructures with a short-range order by means of self-assembly of charged polystyrene beads on the substrate during the mask fabrication step. In the following I will explain the details of the different steps needed to fabricate plasmonic chiral nanostructures.

4. 1. 1. Hole-mask Colloidal Lithography (HCL)

HCL is a technique which can accommodate many tweaks at different steps of its basic recipe; which enables a wide range of nanostructures to be realized (single disk, nanohole, nanoring, dimer, trimer tetramer, cone, elliptical disk, etc.). I will, at first, only describe the fabrication details of regular single gold disks on a glass coverslip. As mentioned before, the advantages of HCL lies in the facility of the method, and in the fact that it allows to obtain a uniform coverage of square centimetres areas. Figure 13 depicts the step-by-step recipe written below.

1. As in every sample preparation in a cleanroom, a clean sample is of utmost importance. To achieve that, the glass coverslip is first blown with a stream of nitrogen to remove the biggest dust particles. It is then followed by three successive ultrasonic baths (Acetone, Isopropanol, Deionized water) lasting 5 minutes each in water at 50 degrees. Finally the coverslip is dried by a stream of nitrogen.
2. The glass, now, has to be topped by a thin layer of PMMA, a light-sensitive polymer. This is done by first covering the whole upper side of the substrate with this polymer, and by spin-coating it. The final thickness of the PMMA will depend on the viscosity of PMMA used, the rotational speed of the spinning, and the time duration of the spinning.
3. To finish evaporation of the remaining solvent in the PMMA, the sample is soft-baked either in an oven or on a hot-plate. The baking temperature should be 180°C and lasts 10 minutes. Following the baking, a light oxygen plasma step (50W, 5s) is required to induce hydrophilicity on the surface of the PMMA layer.
4. The self-assembly is achieved by electrostatic attraction and repulsion between the beads and the surface. To induce surface charges at the surface of PMMA, we deposit a monolayer of a positively charged polyelectrolyte called polydiallyldimethylammonium (PDDA). This polyelectrolyte is spread on the

polymer via pipetting this solution (0,2 % concentration) and has to be left incubating for a certain amount of time (30s) before rinsing (10s) the sample under a constant stream of deionized water. A stream of nitrogen to blow-dry the coverslip will conclude this step.

5. The top of the polymer layer is positively charged, enabling us to add the polystyrene beads. The negatively charged polystyrene beads are found in suspension in aqueous solution, whose concentration and charges content will determine the density of the structures present on your substrate at the end of the recipe. This step is similar to the previous one. With a pipette, the solution of polystyrene beads is spread on the sample surface and left incubating for a certain amount of time (1min), rinsed under a stream of deionized water (30s), and blow-dried under a stream of nitrogen. In this step, the beads will have adhered to the PMMA layer thanks to electrostatic forces; and because each bead has the same charge sign they will repulse each other. This will cause a random monolayer distribution of the beads over the whole surface. The rinsing and drying have the purposes of removing any excess beads still present and prevent any rearrangements of the "fixed" beads.

6. Evaporating a thin metallic layer on top of our sample surface is the next step. This metal layer will form the mask that will be used during a future evaporation step and removed during the lift-off step. Usually the metal evaporated using an electron-gun is either gold or chromium depending on situations. A 10nm-layer thickness of gold is a typical choice.

7. After mask deposition, a tape-stripping process is used to remove the polystyrene beads. After this step, you should be left with a mask perforated by circular holes where the beads were. A good adhesion between the tape and the sample surface is necessary to remove all beads.

8. A long (50W, 2~5min) oxygen plasma etching process will etch away the PMMA not protected by the mask. It will create nanoholes which, with a proper timing of the etching, will reach the glass surface. This timing depends on both the thickness of PMMA one has to go through, and also which shape you wish your nanoholes to have.

9. In this second material evaporation, the desired structures are deposited onto the substrate. Their shapes are dependent on the mask realized previously through steps 6 to 8. Their thicknesses depend on the evaporation length. Here, one can vary the material(s) evaporated to produce different kinds of structures. In our example, gold nanodisks, we are doing a single evaporation at normal incidence.

10. This step is the last in the recipe. Now that our structures are sitting on the surface of the substrate, we need to remove all excess material on top of the PMMA layer as well as the PMMA itself. It is simply done by repeating step 1. Acetone will dissolve PMMA, and all material staying on it will be lifted away. The next ultrasonic baths will complete the cleaning of our now finished sample.

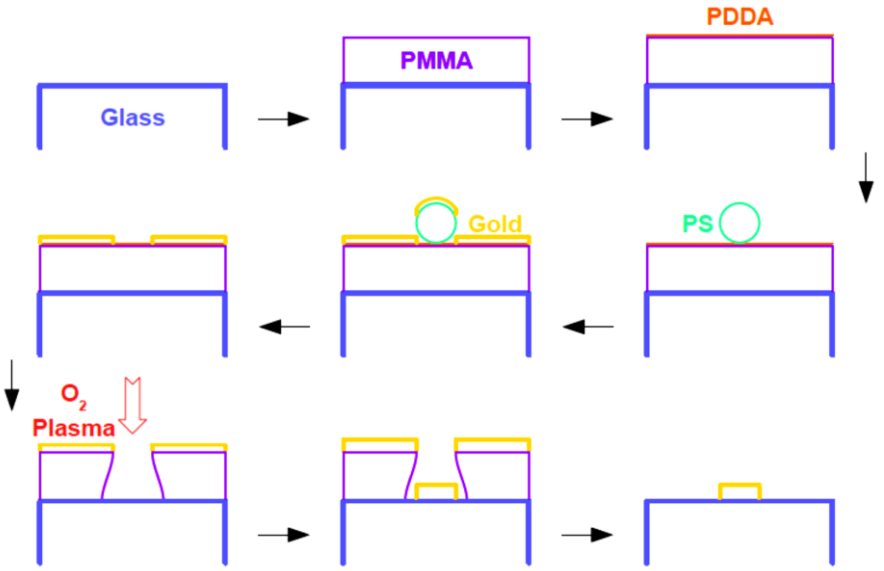

Figure 13: Details step-by-step of the HCL technique to fabricate single gold nanodisks on a glass substrate. Starting from a clean glass coverslip, we spin-coat and soft-bake PMMA polymer. After a brief oxygen plasma, we spread a monolayer of PDDA polyelectrolyte. Then we spread a solution of PS beads with charges opposite to the PDDA, rinse and dry. We evaporate a gold mask, tape-strip away the PS beads, and etch with oxygen plasma again through the PMMA. A second gold evaporation will deposit our nanodisks on the substrate. The sample is finished after the lift-off step and some additional cleaning.

4. 1. 2. Angular evaporation

Adding to the already numerous tools in the cleanroom, the angular evaporation is a tool allowing more variety, but also more complexity, to the structures already available. This process has already proven its versatility in the literature.[44–46] It simply consists in evaporating the material desired with an angle of incidence with respect to the normal of the substrate plane. Indeed, electron-gun evaporation is a technique in which a target, consisting of our material, is bombarded by electrons. With the rising of the target temperature, atoms of the material will start to fly away from it. It will fly away in a directional manner until reaching our sample since the evaporation chamber is under ultra-high vacuum. By enabling to tilt the sample with respect to this evaporation direction, and also enabling the rotation of the sample itself, vast possibilities are opened.

We took advantage of angular evaporation in the fabrication of our chiral nanostructures. However, several parameters have to be taken into considerations: the PMMA layer thickness, the oxygen plasma etching duration of the mask, and the maximum angle of evaporation. Depending on the thickness of the PMMA layer, the duration of the etching has to be adjusted. Since our aim is to be able to evaporate several disks at the bottom of a single nanohole, the diameter of this nanohole at the glass-PMMA interface must be bigger than its diameter at the mask-PMMA interface. To achieve that, one must "over-etch". Both mask- and substrate-side hole diameters and PMMA thickness will define our maximum evaporation angle according to simple trigonometry. Figure 14 illustrates what happens when the evaporation angle is larger than allowed. We can clearly see the demarcation line of the bottom diameter of the nanoholes.

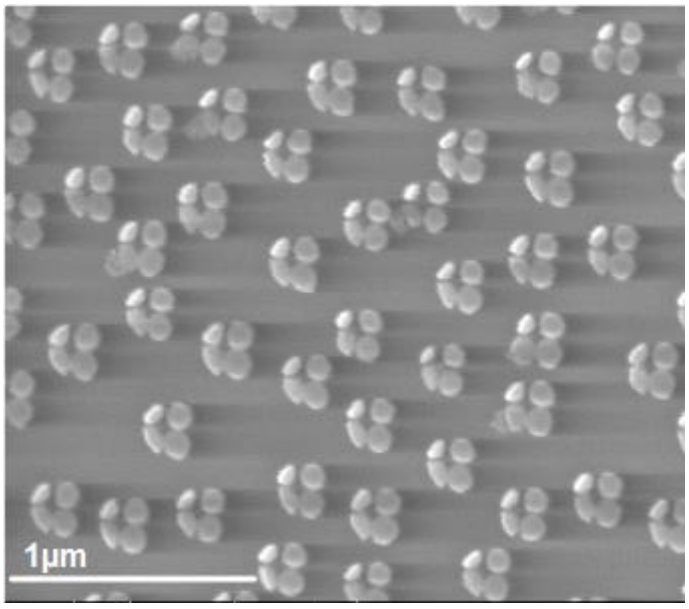

Figure 14: SEM image of gold tetramer nanostructures. The leftmost disks of each structure are misshapen due to the limited size of the bottom hole diameter and a too high evaporation angle.

Because of the possibility to rotate the sample itself, we are able to do sequential evaporation of disks of different materials and/or different heights. The number of disks is controlled as well to the limit of the space available on the substrate. In the case of multiple disks evaporation, we have to be careful about the selection of the evaporation angle to avoid disks overlapping.

4. 1. 3. Chiral nanostructures fabrication protocol

Based on both the HCL technique and angular evaporation, it is then possible to fabricate artificial chiral nanostructures. Starting from the recipe detailed in paragraph 4. 1. 1. , we bring the following modifications to the steps described for the fabrication of silver tetramer:

2. For this step, PMMA-A4 is the polymer of choice for a spin-coating lasting 1 min at 3000 rpm. The resulting PMMA layer after soft-baking should have a thickness around 230 nm.

5. An aqueous solution containing PS beads with an average diameter of 110 nm at a concentration of 0,02 % is used.

8. An oxygen plasma etching at 50W during 3 min would be sufficient to etch a hole through the PMMA and reach the glass substrate. However, since we want to make tetramers and fit 4 disks at the bottom of this hole, we need to over-etch. Thus, we opt for an oxygen plasma etching at 50W during 5 min.

9. Using angular evaporation, silver is evaporated at an angle of 12~13 degrees until reaching the thickness chosen for the first disk. The whole sample is then rotated 90 degrees before the start of the second silver evaporation, etc. Metallic angular evaporation and substrate rotation (at 0, 90, 180, and 270 degrees) are successively repeated until obtaining the 4 silver disks composing our tetramer.

Applying these directives will lead to the fabrication of reproducible chiral nanostructures. We can clearly see how simple it is to modify the HCL technique to achieve radically different nanostructures. It proves how versatile and robust HCL is.

4. 2. Optical characterization

4. 2. 1. Circular Dichroism (CD) measurement

Circular dichroism spectroscopy is generally used to characterize optically active chiral molecules. We copied the measurement principle from a commercial CD spectrometer to realize our own transmission setup able to perform CD measurements. In a commercial CD spectrometer, light is emitted by a high intensity light-source. The collimated light beam passes through a monochromator and a linear polarizer before being turned into either right- or left-circularly polarized light by a photo-elastic modulator (PEM). This PEM is equivalent to a dynamic quarter-wave plate and will produce alternatively right- and left-circularly polarized light at a frequency equal to its driving frequency (~50 kHz). After going through the sample at normal incidence, the light intensity is recorded by a light detector. A lock-in amplifier synchronized to the frequency of the PEM allows to follow the variations in the light transmission intensities between RCP and LCP light. This signal is called *vAC* (in Volts). The average transmitted light intensity over time will give the value *vDC* (in Volts). From these two values, the CD spectrum can be extracted by the formula $CD = \left(\frac{vAC}{vDC}\right) G$, where G is a calibrating factor, over a specified range of wavelengths.

Our transmission setup is a simplified version. A fibre-coupled halogen lamp is used as the light source. This collimated white light passes through a linear polarizer and an achromatic quarter-wave plate which are tuned to obtain either RCP or LCP light. The light beam impinges at a normal incidence with the sample, and the transmitted light is collected and analysed by a fibre-coupled grating spectrometer. In this case, we obtain the CD spectrum using the formula:

$$CD\ (rad) = \frac{T_{RCP}^{1/2} - T_{LCP}^{1/2}}{\frac{1}{2}(T_{RCP}^{1/2} + T_{LCP}^{1/2})} \tag{16}$$

, where T_{RCP} (respectively T_{LCP}) is the normalized transmitted light upon illumination from RCP (respectively LCP) light. This setup is preferably adopted with respect to the commercial CD spectrometer in our case to assure a precise alignment and an exact incident angle of the samples during the measurements.

4. 3. Simulation methods

Artificial chiral structures are complex to understand. Simulating them can enlighten our understanding of the underlying mechanisms behind the different interactions occurring. Two simulation methods have been chosen to perform this task: the coupled-dipole approximation (CDA) method, and the finite element method (FEM). Comparison of their results allows to paint a more complete picture due to our knowledge of their respective limitations.

4. 3. 1. Coupled-Dipole Approximation (CDA)

CDA allows to simulate a system composed of a set of interacting nanoparticles. This set can be ordered or disordered. Each nanoparticle is represented by a point-dipole. From this point-dipole approximation comes some limitations of the CDA method; particle interactions are underestimated when they are in close proximity, and quadrupolar interactions are ignored. Each particle is assumed to be an ellipsoid. According to the modified long wavelength approximation (MLWA) described by Jensen,[47] their MLWA polarizability can be written as:

$$\tilde{\alpha}_{j,ii} = \frac{\alpha_{ii}}{\left(1 - \frac{2}{3} ik^3 \alpha_{ii} - \frac{k^2}{s_i} \alpha_{ii}\right)} \tag{17}$$

, where the polarizability tensor $\tilde{\alpha}_j$ associated to the particle j is described by

$$\tilde{\alpha}_j = \begin{bmatrix} \tilde{\alpha}_{j,xx} & 0 & 0 \\ 0 & \tilde{\alpha}_{j,yy} & 0 \\ 0 & 0 & \tilde{\alpha}_{j,zz} \end{bmatrix} \tag{18}$$

α_{ii} in equation (17) represents the quasi-static polarizability components of an ellipsoid with radii $s_i = a, b, c$ along the axes $i = x, y, z$, respectively.

$$\alpha_{ii} = abc \frac{\varepsilon - n^2}{3n^2 + 3L_i(\varepsilon - n^2)} \tag{19}$$

ε is the complex dielectric function of the ellipsoid, and n is the refractive index of the surrounding medium. L_i is the ellipsoid shape factor and is equal to:

$$L_i = \frac{abc}{2} \int_0^\infty \frac{dq}{(s_i^2 + q)\sqrt{(q + a^2)(q + b^2)(q + c^2)}} \tag{20}$$

From the expression of the polarizability tensor $\tilde{\alpha}_j$ that has been assumed to be diagonal, we can try to solve the coupled dipole equation upon which the coupled-dipole approximation is based:

$$\boldsymbol{P}_j = \tilde{\alpha}_j \boldsymbol{E}_j = \tilde{\alpha}_j \left(\boldsymbol{E}_{inc,j} - \sum_{k \neq j} \boldsymbol{A}_{jk} \boldsymbol{P}_k \right) \tag{21}$$

$\boldsymbol{P}_j$ represents the point-dipoles located at positions $\boldsymbol{r}_j$, and $\boldsymbol{E}_j$ is the local electric field. $\boldsymbol{E}_j$ can be decomposed into the incident plane wave field $\boldsymbol{E}_{inc,\,j}$ and the sum of the retarded induced dipole field - $\boldsymbol{A}_{jk}\boldsymbol{P}_k$ by a particle k at a position j.

$$\boldsymbol{E}_{inc,j} = \boldsymbol{E}_0 \exp\left(i\boldsymbol{k} \,.\, \boldsymbol{r}_j - i\omega t\right) \tag{22}$$

And $\boldsymbol{A}_{jk}$ is a 3×3 matrix which, for $j \neq k$, is equal to:

$$\boldsymbol{A}_{jk} = \frac{\exp(ikr_{jk})}{r_{jk}} \times \left(k^2 \left(\hat{\mathrm{r}}_{jk} \hat{\mathrm{r}}_{jk} - \mathbf{1}_3 \right) + \frac{ikr_{jk} - 1}{r_{jk}^2} \left(3\hat{\mathrm{r}}_{jk} \hat{\mathrm{r}}_{jk} - \mathbf{1}_3 \right) \right) \tag{23}$$

, where $k \equiv \omega/c_0 n$, $r_{jk} = |\boldsymbol{r}_j - \boldsymbol{r}_k|$, $\hat{r}_{jk} \equiv (\boldsymbol{r}_j - \boldsymbol{r}_k)/r_{jk}$, $\mathbf{1}_3$ is the 3×3 identity matrix.

By defining $\boldsymbol{A}_{jj} \equiv \bar{\alpha}_j^{-1}$ the scattering problem reduces to a problem of $3N$ complex linear equations:

$$\sum_{k=1}^{N} \boldsymbol{A}_{jk}\boldsymbol{P}_k = \boldsymbol{E}_{inc,j} \tag{24}$$

, where N is the total number of dipoles in the system. By solving this equation, one can calculate the extinction, absorption, and scattering cross-sections according to:

$$C_{ext} = \frac{4\pi k}{|\boldsymbol{E}_{inc}|^2} \sum_{j=1}^{N} Im\left(\boldsymbol{E}_{inc,j}^{*}.\boldsymbol{P}_j\right) \tag{25.a}$$

$$C_{abs} = \frac{4\pi k}{|\boldsymbol{E}_{inc}|^2} \sum_{k=1}^{N} \left(Im\left[\boldsymbol{P}_j.\left(\alpha_j^{-1}\right)^{*}\boldsymbol{P}_j^{*}\right] - \frac{2}{3}k^3\left|\boldsymbol{P}_j\right|^2 \right) \tag{25.b}$$

$$C_{scatt} = C_{ext} - C_{abs} \tag{25.c}$$

These above-mentioned equations were used to simulate an ensemble of 4 dipoles corresponding to a single tetramer structure. The CD spectrum behaviour of both simulation and experiment were similar, but the CD values were much lower using the CDA than found with the FEM and experiments. As seen in the Appended Paper II, these discrepancies in values are due to the fact that dipole-quadrupole interactions participate in the optical activity of the tetramer, and interparticle distance is important in the near-field coupling of the different disks. Both of these aspects are limitations of the CDA that we mentioned earlier.

4. 3. 2. Finite Elements Method (FEM)

The FEM is a powerful method used in finding solutions to electromagnetic problems in plasmonics and nanophotonics in general. It is based on discretizing the whole simulation domain with a specific mesh. Both scatterers and surrounding medium are discretized. The advantages come from the adaptability of the mesh size and shape to the type and location of investigations made. Of course, the great number of elements results in a consequent simulation time. In Comsol, computation finds numerical approximations of solutions to partial differential equations in each of the domains defined by the mesh. These domains are linked by complex boundary conditions such as: continuity of the tangential components of the fields, transparent boundaries for incident and scattering waves, etc. A good understanding of these boundary conditions, and mesh size allows to get an accurate simulation of the modelled structure.

Chapter 5

Summary and Outlook

5. 1. Summary of appended papers

Appended Paper I, *Ultrafast spinning of gold nanoparticles in water using circularly polarized light*, is a report about the rotation of gold colloids which are trapped in circularly polarized near-infrared laser tweezers. Even though rotation of metallic nanostructures thanks to polarization has already been done before, it is the first time that such a high spinning frequency has been reached. The paper puts in evidence the relation between the transfer of the spin angular momentum of light and the particle absorption. A clear increase in the spinning frequency is observable when the laser power is increased. The observation of the rotation was possible thanks to an APD, whose sensitivity allowed to track small variations in the collected light intensities. These small variations couldn't have occurred without the imperfections in the shape of our gold colloids. By fitting an auto-correlation function to the data collected by the APD, two things can be identified: the spinning frequency, the presence of "noise" in our intensity signal. The latter is attributable to the stochastic torque imposed by the surrounding medium (water) on the trapped bead. A correlation time τ_0 characterises it in the auto-correlation function. An observation of the decrease of this correlation time with respect to an increase in the laser power points to the fact that the viscosity of the surrounding medium is lesser at higher laser power. It suggests an increase in the temperature in the vicinity of the trapped particle. However there is still some uncertainty on the exact amount of influence of this effect.

Appended Paper II, *Macroscopic layers of chiral plasmonic nanoparticle oligomers from colloidal lithography*, is a study of artificial chiral plasmonic structures composed of three to four nanodisks each fabricated based on the technique of hole-mask colloidal lithography and angular metallic evaporation. We observed a very strong chiral optical activity in these oligomers in the visible to near-infrared wavelength range. This optical activity is measured by a method borrowed from biology and chemistry called circular dichroism. It measures the difference in transmitted light intensities when the sample is illuminated by RCP and LCP light. The maximum observed was a difference of 7 % from a sample covered with silver tetramers. To understand the origins of such activity, the tetramers (which are four disks of increasing heights placed on a square base) were simulated and compared with two methods: CDA, and FEM. The limitations of CDA allowed us to isolate some interaction contribution when comparing the simulations to the more complete picture given by FEM. From our analysis, we identified that the dipolar plasmons of the two thinner disks were dominating the CD spectrum at long wavelengths. At shorter wavelengths, contributions are a mix of quadrupolar modes, and dipolar plasmons from the two taller disks. Near-field coupling between the disks is a vital point that is underestimated by CDA. A second criteria is necessary to have an optically active structure; the nanostructure must

have a particular arrangement in 3D such that its overall geometry symmetry is broken. For the purpose of future applications in enantiomer-sensing for example, we used the hole-mask colloidal lithograpy which allows the coverage of large areas relatively easily. Moreover, we created a nanostructure offering multiple gaps where potential "hot spots" could give large enhancements. The *optical chirality* induced by superchiral fields in these hot spots was calculated to see their sensing potential. Despite high values reached, the average value of the optical chirality for the whole nanostructure sensing volume didn't bode well for the enhacement of molecular chirality. The CD of the plasmonic structures themselves would dominate the overall signal.

5. 2. Outlook

In Appended Paper I, we demonstrated that high spinning frequency is achievable in optical trapping simply with circularly polarized light. As optical tweezers are a common tool among biologists, such a possibility makes more accessible their use towards temperature sensing or local viscosity measurement in living samples. The effects occurring to trapped objects spinning at high frequencies, though, have not been fully understood. We identified the viscosity of the surrounding medium as a limiting factor, as well as a temperature increase of the particle. But since such rotating speeds haven't been reached before, some exotic behaviors out of our usual expectations could take place. Alternative means of the nanoparticle observation should be put into place to investigate this subject.

In Appended Paper II, we showed that it was possible to obtain strong circular dichroism in the visible and near-infrared wavelength range thanks to our oligomers. The use of comparative simulation methods opened the interpretation of complex interactions. Different paths are available for us to take. Enantiomer-sensing is still of interest, but we have already seen that our design is not adapted to the task. A possibility would be to fabricate a nanostructure generating superchiral fields with only one handedness. It would enable us to overcome the averaging effect of the optical chirality over the entire nanostructure. Thus, the molecular chirality would be enhanced enough to compete with the optical activity of the plasmonic oligomer itself. The versatility of our fabrication approach, though, has been demonstrated. This versatility could be used to make chiral nanostructures out of several metals for example.

Another possibility would be combining what we learnt from both Appended Papers. Inspired from the experiment by Beth in 1936,[23] it would be interesting to observe mechanical rotation of a metamaterial sample, fabricated along the lines of our proven fabrication techniques, and set into movement by the polarization of laser tweezers.

Acknowledgments

Finishing this thesis wouldn't have been possible without the help from many people which I would like to thank:

First of all, my supervisor, Mikael Käll, for the guidance through the past years, all the advices provided both in research and in writing papers, and for all the opportunities. My co-supervisor, Peter Johansson, for the theoretical understanding that you brought, and the help in articles. Thank you Anni for all the hard work in the project we shared. Thanks to Yurui for the lengthy simulations you had to repeat multiple times. Thank you Mikael, for you measurement expertise. Thanks Vlada, Si and Zhaleh for introducing me to colloidal lithography. Thanks Julia Fernandez-Rodriguez, for your enthusiasm at the CCI.

The whole Bionanophotonics group. We are so large right now! But I still enjoy the open atmosphere that hovers around. Si and Yurui, for sharing the same office. Vlada, Kristof, Mikael, Anni, and Gülis, for the travels we shared over the world. Thanks to Mokhtar, Virginia and Ruggero for the dinners, picnics, etc. we had at multiple occasions. Aron, for your passion of whisky. Andreas, for opening your house to games. Timur, and Kristof, always ready to try new experiments or samples.

Thanks to Michelle, which became such a big part of my life now.

Finally, many thanks to my family, which always supported me during all my studies and my decisions, wherever it would lead me to.

Bibliography

(1) Maier, S. A. *Plasmonics: Fundamentals and Applications*; Springer, 2007; p. 224.

(2) Ozbay, E. Plasmonics: Merging Photonics and Electronics at Nanoscale Dimensions. *Science* **2006**, *311*, 189–193.

(3) Csaki, A.; Schneider, T.; Wirth, J.; Jahr, N.; Steinbrück, A.; Stranik, O.; Garwe, F.; Müller, R.; Fritzsche, W. Molecular Plasmonics: Light Meets Molecules at the Nanoscale. *Philos. Trans. A. Math. Phys. Eng. Sci.* **2011**, *369*, 3483–3496.

(4) Ming, T.; Zhao, L.; Yang, Z.; Chen, H.; Sun, L.; Wang, J.; Yan, C. Strong Polarization Dependence of Plasmon-Enhanced Fluorescence on Single Gold Nanorods. *Nano Lett.* **2009**, *9*, 3896–3903.

(5) Thompson, P. G.; Biris, C. G.; Osley, E. J.; Gaathon, O.; Osgood, R. M.; Panoiu, N. C.; Warburton, P. A. Polarization-Induced Tunability of Localized Surface Plasmon Resonances in Arrays of Sub-Wavelength Cruciform Apertures. *Opt. Express* **2011**, *19*, 25035–25047.

(6) Song, M.; Chen, G.; Liu, Y.; Wu, E.; Wu, B.; Zeng, H. Polarization Properties of Surface Plasmon Enhanced Photoluminescence from a Single Ag Nanowire. *Opt. Express* **2012**, *20*, 22290–22297.

(7) Lin, J.; Mueller, J. P. B.; Wang, Q.; Yuan, G.; Antoniou, N.; Yuan, X.-C.; Capasso, F. Polarization-Controlled Tunable Directional Coupling of Surface Plasmon Polaritons. *Science* **2013**, *340*, 331–334.

(8) Joly, Y. *Interaction of Polarized Light with Matter*; Beaurepaire, E.; Bulou, H.; Scheurer, F.; Jean-Paul, K., Eds.; Springer Proceedings in Physics; Springer Berlin Heidelberg: Berlin, Heidelberg, 2010; Vol. 133, pp. 77–125.

(9) Campos-Fernández, C.; Azofeifa, D. E.; Hernández-Jiménez, M.; Ruiz-Ruiz, A.; Vargas, W. E. Visible Light Reflection Spectra from Cuticle Layered Materials. *Opt. Mater. Express* **2011**, *1*, 85–100.

(10) Hendry, E.; Carpy, T.; Johnston, J.; Popland, M.; Mikhaylovskiy, R. V; Lapthorn, A. J.; Kelly, S. M.; Barron, L. D.; Gadegaard, N.; Kadodwala, M. Ultrasensitive Detection and Characterization of Biomolecules Using Superchiral Fields. *Nat. Nanotechnol.* **2010**, *5*, 783–787.

(11) Dholakia, K.; Reece, P.; Gu, M. Optical Micromanipulation. *Chem. Soc. Rev.* **2008**, *37*, 42–55.

(12) Dienerowitz, M. Optical Manipulation of Nanoparticles: A Review. *J. Nanophotonics* **2008**, *2*, 021875.

(13) Neuman, K. C.; Nagy, A. Single-Molecule Force Spectroscopy: Optical Tweezers, Magnetic Tweezers and Atomic Force Microscopy. *Nat. Methods* **2008**, *5*, 491–505.

(14) Perkins, T. T. Optical Traps for Single Molecule Biophysics: A Primer. *Laser Photonics Rev.* **2009**, *3*, 203–220.

(15) Min, C.; Shen, Z.; Shen, J.; Zhang, Y.; Fang, H.; Yuan, G.; Du, L.; Zhu, S.; Lei, T.; Yuan, X. Focused Plasmonic Trapping of Metallic Particles. *Nat. Commun.* **2013**, *4*, 2891.

(16) Tong, L.; Miljković, V. D.; Käll, M. Alignment, Rotation, and Spinning of Single Plasmonic Nanoparticles and Nanowires Using Polarization Dependent Optical Forces. *Nano Lett.* **2010**, *10*, 268–273.

(17) Hentschel, M.; Schäferling, M.; Weiss, T.; Liu, N.; Giessen, H. Three-Dimensional Chiral Plasmonic Oligomers. *Nano Lett.* **2012**, *12*, 2542–2547.

(18) Fredriksson, H.; Alaverdyan, Y.; Dmitriev, A.; Langhammer, C.; Sutherland, D. S.; Zäch, M.; Kasemo, B. Hole–Mask Colloidal Lithography. *Adv. Mater.* **2007**, *19*, 4297–4302.

(19) Dienerowitz, M.; Mazilu, M.; Reece, P. J.; Krauss, T. F.; Dholakia, K. Optical Vortex Trap for Resonant Confinement of Metal Nanoparticles. *Opt. Express* **2008**, *16*, 4991–4999.

(20) Friese, M. E. J.; Enger, J.; Rubinsztein-Dunlop, H.; Heckenberg, N. R. Optical Angular-Momentum Transfer to Trapped Absorbing Particles. *Phys. Rev. A* **1996**, *54*, 1593–1596.

(21) Lehmuskero, A.; Li, Y.; Johansson, P.; Käll, M. Plasmonic Particles Set into Fast Orbital Motion by an Optical Vortex Beam. *Opt. Express* **2014**, *22*, 4349–4356.

(22) Toyoda, K.; Miyamoto, K.; Aoki, N.; Morita, R.; Omatsu, T. Using Optical Vortex to Control the Chirality of Twisted Metal Nanostructures. *Nano Lett.* **2012**, *12*, 3645–3649.

(23) Beth, R. A. Mechanical Detection and Measurement of the Angular Momentum of Light. *Phys. Rev.* **1936**, *50*, 115–125.

(24) Ashkin, A.; Dziedzic, J. M.; Bjorkholm, J. E.; Chu, S. Observation of a Single-Beam Gradient Force Optical Trap for Dielectric Particles. *Opt. Lett.* **1986**, *11*, 288–290.

(25) Novotny, L.; Hecht, B. *Principles of Nano-Optics*; Cambridge University Press, 2012; p. 559.

(26) Loudon, R.; Barnett, S. M. Theory of the Radiation Pressure on Dielectric Slabs, Prisms and Single Surfaces. *Opt. Express* **2006**, *14*, 11855–11869.

(27) Barnett, S. M.; Allen, L. Orbital Angular Momentum and Nonparaxial Light Beams. *Opt. Commun.* **1994**, *110*, 670–678.

(28) Simpson, N. B.; Dholakia, K.; Allen, L.; Padgett, M. J. Mechanical Equivalence of Spin and Orbital Angular Momentum of Light: An Optical Spanner. *Opt. Lett.* **1997**, *22*, 52–54.

(29) Pesce, G.; Sasso, A.; Fusco, S. Viscosity Measurements on Micron-Size Scale Using Optical Tweezers. *Rev. Sci. Instrum.* **2005**, *76*, 115105.

(30) Bendix, P. M.; Reihani, S. N. S.; Oddershede, L. B. Direct Measurements of Heating by Electromagnetically Trapped Gold Nanoparticles on Supported Lipid Bilayers. *ACS Nano* **2010**, *4*, 2256–2262.

(31) Govorov, A. O.; Richardson, H. H. Generating Heat with Metal Nanoparticles. *Nanotoday* **2007**, *2*, 30–38.

(32) Fang, Z.; Zhen, Y.-R.; Neumann, O.; Polman, A.; García de Abajo, F. J.; Nordlander, P.; Halas, N. J. Evolution of Light-Induced Vapor Generation at a Liquid-Immersed Metallic Nanoparticle. *Nano Lett.* **2013**, *13*, 1736–1742.

(33) Genevet, P.; Yu, N.; Aieta, F.; Lin, J.; Kats, M. A.; Blanchard, R.; Scully, M. O.; Gaburro, Z.; Capasso, F. Ultra-Thin Plasmonic Optical Vortex Plate Based on Phase Discontinuities. *Appl. Phys. Lett.* **2012**, *100*, 013101.

(34) Karimi, E.; Schulz, S. A.; De Leon, I.; Qassim, H.; Upham, J.; Boyd, R. W. Generating Optical Orbital Angular Momentum at Visible Wavelengths Using a Plasmonic Metasurface. *Light Sci. Appl.* **2014**, *3*, e167.

(35) Marston, P. L.; Crichton, J. H. Radiation Torque on a Sphere Caused by Circularly-Polarized Electromagnetic Wave. *Phys. Rev. A* **1984**, *30*, 2508–2516.

(36) Liu, M.; Zentgraf, T.; Liu, Y.; Bartal, G.; Zhang, X. Light-Driven Nanoscale Plasmonic Motors. *Nat. Nanotechnol.* **2010**, *5*, 570–573.

(37) Choi, J. S.; Cho, M. Limitations of a Superchiral Field. *Phys. Rev. A* **2012**, *86*, 063834.

(38) Tang, Y.; Cohen, A. E. Optical Chirality and Its Interaction with Matter. *Phys. Rev. Lett.* **2010**, *104*, 163901.

(39) Lipkin, D. M. Existence of a New Conservation Law in Electromagnetic Theory. *J. Math. Phys.* **1964**, *5*, 696.

(40) Tang, Y.; Cohen, A. E. Enhanced Enantioselectivity in Excitation of Chiral Molecules by Superchiral Light. *Science* **2011**, *332*, 333–336.

(41) Davis, T.; Hendry, E. Superchiral Electromagnetic Fields Created by Surface Plasmons in Nonchiral Metallic Nanostructures. *Phys. Rev. B* **2013**, *87*, 085405.

(42) Meinzer, N.; Hendry, E.; Barnes, W. L. Probing the Chiral Nature of Electromagnetic Fields Surrounding Plasmonic Nanostructures. *Phys. Rev. B* **2013**, *88*, 041407.

(43) Schäferling, M.; Yin, X.; Engheta, N.; Giessen, H. Helical Plasmonic Nanostructures as Prototypical Chiral Near-Field Sources. *ACS Photonics* **2014**, *1*, 530–537.

(44) Dietrich, K.; Lehr, D.; Helgert, C.; Tünnermann, A.; Kley, E.-B. Circular Dichroism from Chiral Nanomaterial Fabricated by on-Edge Lithography. *Adv. Mater.* **2012**, *24*, OP321–5.

(45) Frank, B.; Yin, X.; Schäferling, M.; Zhao, J.; Hein, S. M.; Braun, P. V; Giessen, H. Large-Area 3D Chiral Plasmonic Structures. *ACS Nano* **2013**, *7*, 6321–6329.

(46) Shegai, T.; Chen, S.; Miljković, V. D.; Zengin, G.; Johansson, P.; Käll, M. A Bimetallic Nanoantenna for Directional Colour Routing. *Nat. Commun.* **2011**, *2*, 481.

(47) Jensen, T.; Kelly, L.; Lazarides, A.; Schatz, G. C. Electrodynamics of Noble Metal Nanoparticles and Nanoparticle Clusters. *J. Clust. Sci.* **1999**, *10*, 295–317.